An effective method towards large field-of-view gamma-ray computed tomography based on an inverse Compton scattering light source*

Zhijun Chi,[1,†] Hongze Zhang,[2] Jiayi Sun,[2] Hao Ding,[2] Jin Lin,[2] Xuanqi Zhang,[2] Qili Tian,[2] Zhi Zhang,[2] Yingchao Du,[2] Wenhui Huang,[2] and Chuanxiang Tang[2]

[1] *Key Laboratory of Beam Technology of Ministry of Education, School of Physics and Astronomy, Beijing Normal University, Beijing 100875, China*

[2] *Key Laboratory of Particle and Radiation Imaging of Ministry of Education, Department of Engineering Physics, Tsinghua University, Beijing 100084, China*

The quasi-monochromatic, continuously energy-tunable, and high-brightness gamma-rays produced by an inverse Compton scattering (ICS) light source provide an ideal probe for gamma-ray imaging. However, due to the influence of the intrinsic energy-angle correlation spectrum of this type of light source, a monochromatic computed tomography (CT), especially in the gamma-ray energy region, can only be realized in a low-efficient way as the first generation CT. To improve the imaging efficiency, a dual-energy scan scheme with large imaging field-of-view (FOV) was developed in this paper. The effectiveness of this scheme was demonstrated based on beam parameters of a typical ICS light source using Monte Carlo simulations. Taking advantage of the principle of basis material decomposition, the influence of energy-angle correlation spectrum on CT reconstruction was corrected, and monochromatic CT of the imaging object was accurately reconstructed. Furthermore, the electron density and effective atomic number of the imaging object can be obtained at the same time.

Keywords: Gamma-ray computed tomography, Energy-angle correlation, Basis material decomposition, Inverse Compton scattering light source, Monte Carlo simulation

I. INTRODUCTION

Since 1980s, computed tomography (CT) technique has been developed into a powerful tool for industrial non-destructive testing (NDT), where the structure integrity of assembled devices is assessed and the quality of manufactured components is inspected. In those NDT applications, the main focus is qualitative feature recognition (or visualization), such as flaw detection, morphological characterization of internal structures, and material wear inspection. With the development of the state-of-the-art precision engineering (e.g., additive manufacturing [1, 2]), there is an increasing demand for accurate dimensional measurement to assure the manufacturing quality (e.g., wall thickness, pore size, geometry tolerance verification, etc.) without destroying the part, and CT technique plays a significant role in the dimensional metrology [3–6], especially for dimensional determination of internal or hidden structures of a component.

In an industrial CT system, X-rays are, in general, produced by the so-called bremsstrahlung—a process where high energy electrons are braked by an anode and a continuous spectrum is produced. Since the X-ray absorption of a material is energy-dependent, beam hardening artifacts will occur when a polychromatic spectrum is used in CT reconstruction. Owing to the influence of beam hardening artifacts, serious errors will be caused in the dimensional measurements [7–11], hampering the accurately quantitative analysis and inspection. Several methods have been developed to correct this influence since the invention of CT technique. However, those correction algorithms have their own limitations, for example, the reduction of photon flux by pre-filtering, the requirement of prior knowledge of imaging materials or spectrum [8, 10, 12–22], two scans at preferably non-overlapping spectra [23, 24], and computational complexity [21, 22, 25–28]. To resolve the beam hardening effect fundamentally, it is necessary to develop a monochromatic X-ray source, especially a monochromatic gamma-ray source with a strong-penetration power for industrial high-Z material imaging, characterized by high beam qualities, suitable footprint, and moderate cost.

With the development of high-brightness electron beam and high-power laser, an inverse Compton scattering (ICS, also called Thomson scattering in the low-energy region [29, 30]) gamma-ray source has been developed into an excellent light source for advanced gamma-ray imaging, since it can provide quasi-monochromatic, continuously energy-tunable, small focal spot, and high-brightness gamma-rays [31–33]. Furthermore, the footprint of this type of light source is room-scale or container-scale, making it flexible for clinical or industrial NDT applications. Therefore, ICS light sources have recently drawn much attention in the field of advanced radiation imaging, including monochromatic and spectral imaging [34–37], phase contrast imaging [38–42], polarization-based imaging [43, 44], and nuclear resonance fluorescence imaging [45–49]. For an ICS light source, the gamma-ray photon energy E_γ, in a head-on interaction geometry between the relativistic electron and the laser and considering the relativistic approximation ($\gamma \gg 1$, $\gamma^2 \gg a_0^2$, and $\theta \ll 1$), can be described as [50]

$$E_\gamma = \frac{4\gamma^2 E_l}{1 + a_0^2/2 + (\gamma\theta)^2}, \quad (1)$$

where E_l is the laser photon energy, γ is the relativistic Lorentz factor, a_0 is the magnitude of the normalized laser vector potential and can be neglected in the linear scattering

* Supported by the National Natural Science Foundation of China (Grant Nos. 12375157, 12027902, and 11905011).

† chizj18@bnu.edu.cn

process ($a_0 \ll 1$), and θ is the detection angle between the electron moving direction and the gamma-ray observation direction. Obviously, the gamma-ray energy is correlated with the detection angle. In order to obtain quasi-monochromatic gamma-rays, the detection angle must be confined by a collimator, because of which the field-of-view (FOV) for imaging is very small, especially in the high-energy region where γ is very large and E_γ is more sensitive to the change of θ. For example, for gamma-rays with a peak energy of 2 MeV and generated using a laser with a wavelength of 800 nm, the typical FOV within which the gamma-ray bandwidth is determined only by beam parameters (intrinsic bandwidth, not influenced by the energy-angle correlation) is ∼5 mm or less at 10 m downstream of the interaction point (IP) between the relativistic electron and the laser. Hence, the "translation + rotation" scan scheme of the first generation CT must be used to realize a CT for centimeter-scale objects, which has been proven to be time-consuming.

To improve the imaging efficiency of gamma-ray CT based on ICS light sources, it is necessary to increase the imaging FOV without reducing the beam intensity, which means that special efforts must be paid to correct the influence of intrinsic energy-angle correlation spectrum of this type of light source on the CT reconstruction. In this paper, a dual-energy scan scheme was proposed to realize large FOV gamma-ray CT by taking full advantage of the straightforward energy tunability of ICS light sources. The feasibility of this scheme was investigated based on a typical ICS light source using Monte Carlo simulations.

II. METHODS

A. Principle of gamma-ray dual-energy scan scheme

According to the interaction mechanism between X-ray photons and materials, the linear attenuation coefficient $\mu(E)$ of a material can be decomposed into three parts, i.e.,

$$\mu(E) = a_{\mathrm{PE}} f_{\mathrm{PE}}(E) + a_{\mathrm{CS}} f_{\mathrm{CS}}(E) + a_{\mathrm{PP}} f_{\mathrm{PP}}(E), \quad (2)$$

where $f_{\mathrm{PE}}(E)$, $f_{\mathrm{CS}}(E)$, and $f_{\mathrm{PP}}(E)$ are the energy E dependencies of photoelectric, Compton scattering, and pair production effects, respectively, and the decomposition coefficients a_{PE}, a_{CS}, and a_{PP} are related with the material properties,

$$a_{\mathrm{PE}} = K_1 Z^n \rho \frac{Z}{A}, \quad (3a)$$

$$a_{\mathrm{CS}} = K_2 \rho \frac{Z}{A}, \quad (3b)$$

$$a_{\mathrm{PP}} = K_3 Z \rho \frac{Z}{A}, \quad (3c)$$

where ρ, Z, and A denote the mass density, atomic number, and atomic weight, respectively, K_1, K_2, and K_3 are constants, and $n \approx 3$.

In the low-energy region ($E < 1.022$ MeV), the pair production process cannot occur; hence, only the photoelectric and Compton scattering terms in Eq. (2) contribute to the linear attenuation coefficient $\mu(E)$. For the photoelectric term, $f_{\mathrm{PE}}(E)$ is empirically taken as $1/E^3$ when no electron-shell discontinuity occurs in the consideration energy region, which restricts the model to be applied for very high-Z materials; for the Compton scattering term, $f_{\mathrm{CS}}(E)$ is explicitly described by the well-known Klein-Nishina formula, which assumes the unbound electron and at rest, neglecting the incoherent scattering function and the Doppler broadening, respectively. Using dual-energy CT scan, the projections of a_{PE} and a_{CS} can be calculated, based on which the spatial distribution of a_{PE} and a_{CS} can be reconstructed. Thus, a monochromatic CT of the imaging object can be obtained using Eq. (2) by neglecting the pair production term. This is the principle of dual-energy method for beam hardening correction in the diagnostic X-ray energy region [23, 24] and has been applied to the energy-angle correlation correction for monochromatic CT based on an ICS light source in the keV energy region [35].

In the high-energy region (e.g., hundreds of keV to several MeVs), the contribution of photoelectric effect to the linear attenuation coefficient $\mu(E)$, compared with the Compton scattering and pair production terms, is usually negligible. In principle, the spatial distribution of a_{CS}, and a_{PP} of the imaging object can also be reconstructed by using dual-energy scan. However, there is no explicit expression of $f_{\mathrm{PP}}(E)$ due to the complex energy-dependence of pair production effect. In this case, the basis material decomposition model is often adopted [51].

In the basis material decomposition model, an arbitrary material can be treated as a mixture of two basis materials and its linear attenuation coefficient $\mu(E)$ can be decomposed as

$$\mu(E) = c_1 \mu_{\mathrm{BM},1}(E) + c_2 \mu_{\mathrm{BM},2}(E), \quad (4)$$

where $\mu_{\mathrm{BM},1}(E)$ and $\mu_{\mathrm{BM},2}(E)$ are the linear attenuation coefficients of the two basis materials and their values at any gamma-ray energy are known, and c_1 and c_2 are the decomposition coefficients. When a dual-energy scan is conducted, the projections of linear attenuation coefficient at both high and low gamma-ray energies can be obtained,

$$P_{\mathrm{H}} = -\ln \int_{\mathrm{SpecH}} S(E) \exp\left[-\int_s \mu(\vec{r}, E)\mathrm{d}s\right] \mathrm{d}E, \quad (5a)$$

$$P_{\mathrm{L}} = -\ln \int_{\mathrm{SpecL}} S(E) \exp\left[-\int_s \mu(\vec{r}, E)\mathrm{d}s\right] \mathrm{d}E, \quad (5b)$$

where P_{H} and P_{L} are the measured projections at high- (SpecH) and low-energy (SpecL) spectra, respectively, $\vec{r}$ denotes a position vector in Euclidean space, and $S(E)$ is the intensity-normalized energy spectrum [$\int_{\mathrm{SpecH}} S(E)\mathrm{d}E = 1$ and $\int_{\mathrm{SpecL}} S(E)\mathrm{d}E = 1$], which can be approximated by a Gaussian distribution at any local position of the gamma-ray beam profile for an ICS light source. Since the local bandwidth of an ICS light source is very narrow (typical rms

value is a few percent), $S(E)$, compared with the energy-dependence of $\mu(E)$ in the high-energy region, can be treated as a Dirac function $\delta(E)$. Thus, Eq. (5) can be further simplified as

$$P_{\mathrm{H}} = \int_s \mu(\vec{r}, E_{\mathrm{H}})\mathrm{d}s, \tag{6a}$$

$$P_{\mathrm{L}} = \int_s \mu(\vec{r}, E_{\mathrm{L}})\mathrm{d}s, \tag{6b}$$

with E_{H} and E_{L} being the peak energies of the high- and low-energy spectra, respectively. Combining Eqs. (4) and (6), a linear equation system can be established,

$$\begin{bmatrix} P_{\mathrm{H}} \\ P_{\mathrm{L}} \end{bmatrix} = \begin{bmatrix} \mu_{\mathrm{BM},1}(E_{\mathrm{H}}) & \mu_{\mathrm{BM},2}(E_{\mathrm{H}}) \\ \mu_{\mathrm{BM},1}(E_{\mathrm{L}}) & \mu_{\mathrm{BM},2}(E_{\mathrm{L}}) \end{bmatrix} \begin{bmatrix} C_1 \\ C_2 \end{bmatrix}, \tag{7}$$

with

$$C_1 = \int_s c_1(\vec{r})\mathrm{d}s, \tag{8a}$$

$$C_2 = \int_s c_2(\vec{r})\mathrm{d}s. \tag{8b}$$

Solving the linear equation system Eq. (7), the projections C_1 and C_2 can be calculated. Thus, the projection $P(E)$ of linear attenuation coefficient at an arbitrary energy E can be obtained,

$$P(E) = \int_s \mu(\vec{r}, E)\mathrm{d}s = C_1\mu_{\mathrm{BM},1}(E) + C_2\mu_{\mathrm{BM},2}(E), \tag{9}$$

and a monochromatic CT of the imaging object at the energy E can be obtained by the reconstruction of $P(E)$.

For an ICS light source, the gamma-ray energy can be easily adjusted by changing either the electron energy or the interaction angle between the electron and the laser. Using a dual-energy scan, the influence of energy-angle correlation spectrum, encountered in a large FOV imaging geometry using ICS light sources, on the CT reconstruction can be easily resolved. Although the energy-angle correlation exists in the scan of each gamma-ray peak energy, the local quasi-monochromaticity [$\delta(E)$ approximation] at an arbitrary detection angle of the FOV (or an arbitrary detection position within the gamma-ray beam profile) can be satisfied (also see Fig. 3 for the simulated gamma-ray spectra); hence, two projections at different gamma-ray energies (E_{H} and E_{L}) can be obtained at any detection angle of the FOV. The two gamma-ray energies E_{H} and E_{L} can be calculated using Eq. (1) when the gamma-ray peak energies ($E_{\mathrm{H,max}}$ and $E_{\mathrm{L,max}}$) are determined, based on which the values of $\mu_{\mathrm{BM},1}$ and $\mu_{\mathrm{BM},2}$ can be obtained at the two gamma-ray energies E_{H} and E_{L}. Solving Eq. (7) and using the composition relation Eq. (9), the projections of the imaging object at any detection angle of the FOV can be corrected to the same gamma-ray energy, as illustrated in Fig 1. Therefore, a monochromatic CT of the imaging object can be reconstructed.

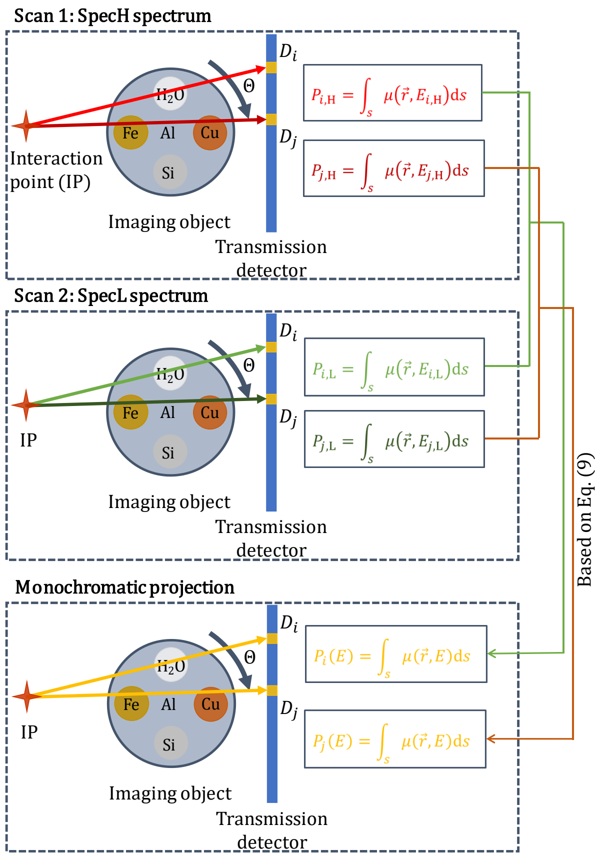

Fig. 1. Dual-energy scan scheme to obtain monochromatic projections of the imaging object at different detector pixels D_i and D_j.

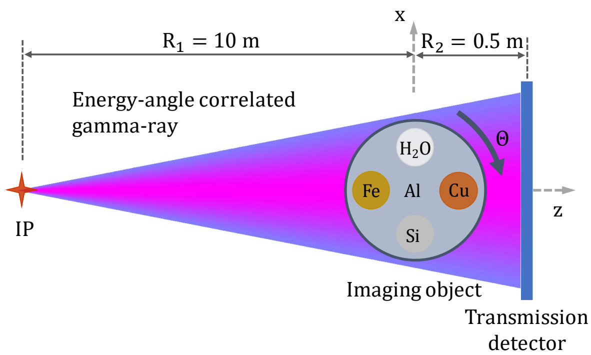

Fig. 2. Imaging layout for large FOV gamma-ray CT based on an ICS light source (not to scale).

B. Monte Carlo simulation

To demonstrate the feasibility of the proposed large FOV gamma-ray CT scheme, Monte Carlo (MC) simulations were carried out using the Geant4 toolkit [52]. The imaging geometry was modeled based on the imaging system constructed

for the very compact ICS gamma-ray source (VIGAS) [53–55] under construction at Tsinghua university. A fan beam geometry was adopted and the imaging layout is shown in Fig. 2. Gamma-ray photons were generated from the IP (gamma-ray spot size 10 μm, rms) and propagated $R_1 = 10$ m to the imaging object. The spectrum of gamma-ray photons, as shown in Fig. 3, was generated from the CAIN [56], a most used MC code for ICS simulation, by taking the practical beam parameters of the VIGAS into account. The gamma-ray peak energies $E_{\mathrm{L,max}}$ and $E_{\mathrm{H,max}}$ of the dual-energy scan were 2 and 4 MeV, respectively. The imaging object was scanned by the two spectra separately. At VIGAS, gamma-rays with a peak energy of 2 and 4 MeV were generated by the interaction of 290 MeV electrons and the lasers with a wavelength of 800 and 400 nm, respectively. The CAIN simulation result of the gamma-ray spectrum was loaded into the Geant4 for further imaging simulation. Both the energy-angle correlation and the energy spread of the spectrum were taken into account in the MC simulation. To acquire the projection data of the imaging object, an ideal transmission detector with pixel size of 0.2 mm was placed at $R_2 = 0.5$ m downstream of the imaging object. For an ICS light source, the photon intensity of generated gamma-rays decreases with the detection angle, as shown in Fig. 3(a). To guarantee the necessary photon intensity at the boundary of the gamma-ray beam profile, the gamma-ray collecting angle θ_c was chosen as $1/\gamma$ ($\sim$1.76 mrad), corresponding to an FOV of $\sim$3.5 cm at the position of the imaging object. Compared with the quasi-monochromatic case (typical FOV $\sim$5 mm or less at 2 MeV), the FOV is increased more than 7-fold in the dual-energy scan scheme.

The imaging object was a aluminum (Al) cylinder with a diameter of 3.0 cm, inside which there were four cylindrical columns with a diameter of 8.0 mm. The four inner columns were made of iron (Fe), copper (Cu), water (H_2O), and silicon (Si), respectively. For the CT scan of the imaging object, the rotation axis was the central axis of the Al cylinder and it was located at the center of the gamma-ray beam.

In the MC simulation, 360 projections evenly distributed in the angular range of 0–360° were acquired for each CT scan. In each projection, 9×10^7 gamma-ray photons were simulated to balance the statistic error and the time cost.

C. Image reconstruction

Based on the dual-energy scan scheme, monochromatic projections of the imaging object at an arbitrary gamma-ray energy E can be obtained using Eq. (9). Monochromatic CT reconstruction of the imaging object at gamma-ray energies of 2 and 4 MeV was realized using the well-known ART-TV iterative algorithm.

Since the monochromatic CTs of the imaging object at gamma-ray energies of 4 and 2 MeV were obtained, the effective atomic number Z_{eff} and electron density ρ_e of the imaging object can also be obtained. Combining Eqs. (2) and (3), the linear attenuation coefficient of a material in the gamma-ray energy region can be written as

$$\mu(E) = g_2 \rho_e f_{\mathrm{CS}}(E) + g_3 Z_{\mathrm{eff}} \rho_e f_{\mathrm{PP}}(E), \tag{10}$$

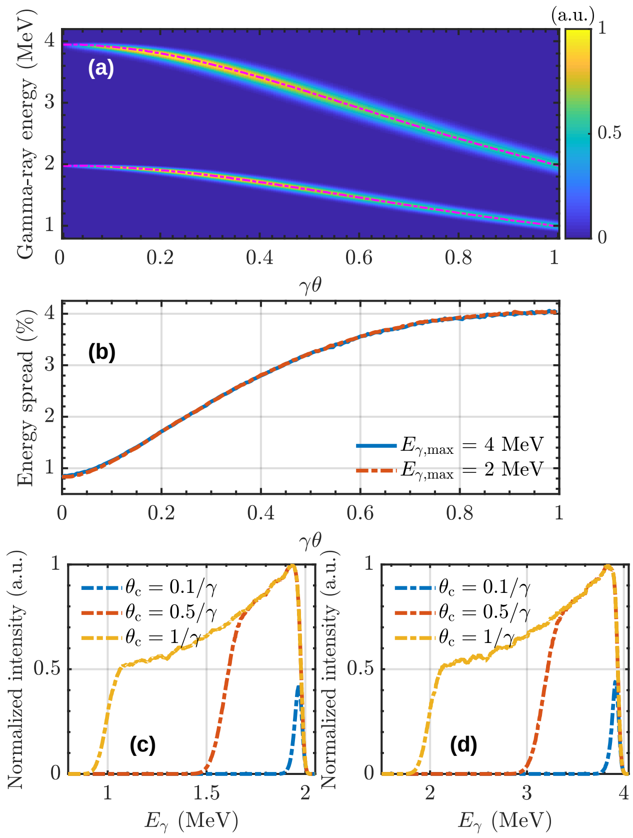

Fig. 3. Simulation spectra of the VIGAS using the CAIN software: (a) angular distribution of the generated gamma-rays, (b) local rms energy spreads at different detection angles (or different detection positions within the gamma-ray beam profile), and the normalized gamma-ray spectra at different collecting angle θ_c for $E_{\gamma,\max} = 2$ MeV (c) and 4 MeV (d), respectively. The pink dotted lines in (a) are the theoretical results obtained from Eq. (1). Although the gamma-ray energy spread increases with the detection angle, the spectrum is still very narrow that it can be considered to be quasi-monochromatic at different detection angles.

where g_2 and g_3 are constants related to K_2 and K_3, respectively, and ρ_e is defined as

$$\rho_e = \rho \frac{Z}{A} N_{\mathrm{A}}, \tag{11}$$

with N_{A} being the Avogadro's constant. Further considering the basis material decomposition model Eq. (4), the electron density ρ_e and effective atomic number Z_{eff} of a material can be written as

$$\rho_e = c_1 \rho_{e,1} + c_2 \rho_{e,2}, \tag{12a}$$

$$Z_{\mathrm{eff}} = \frac{c_1 Z_1 \rho_{e,1} + c_2 Z_2 \rho_{e,2}}{\rho_e}, \tag{12b}$$

where Z_i and $\rho_{e,i}$ ($i = 1$ or 2) are, respectively, the known atomic number and electron density of the ith basis material.

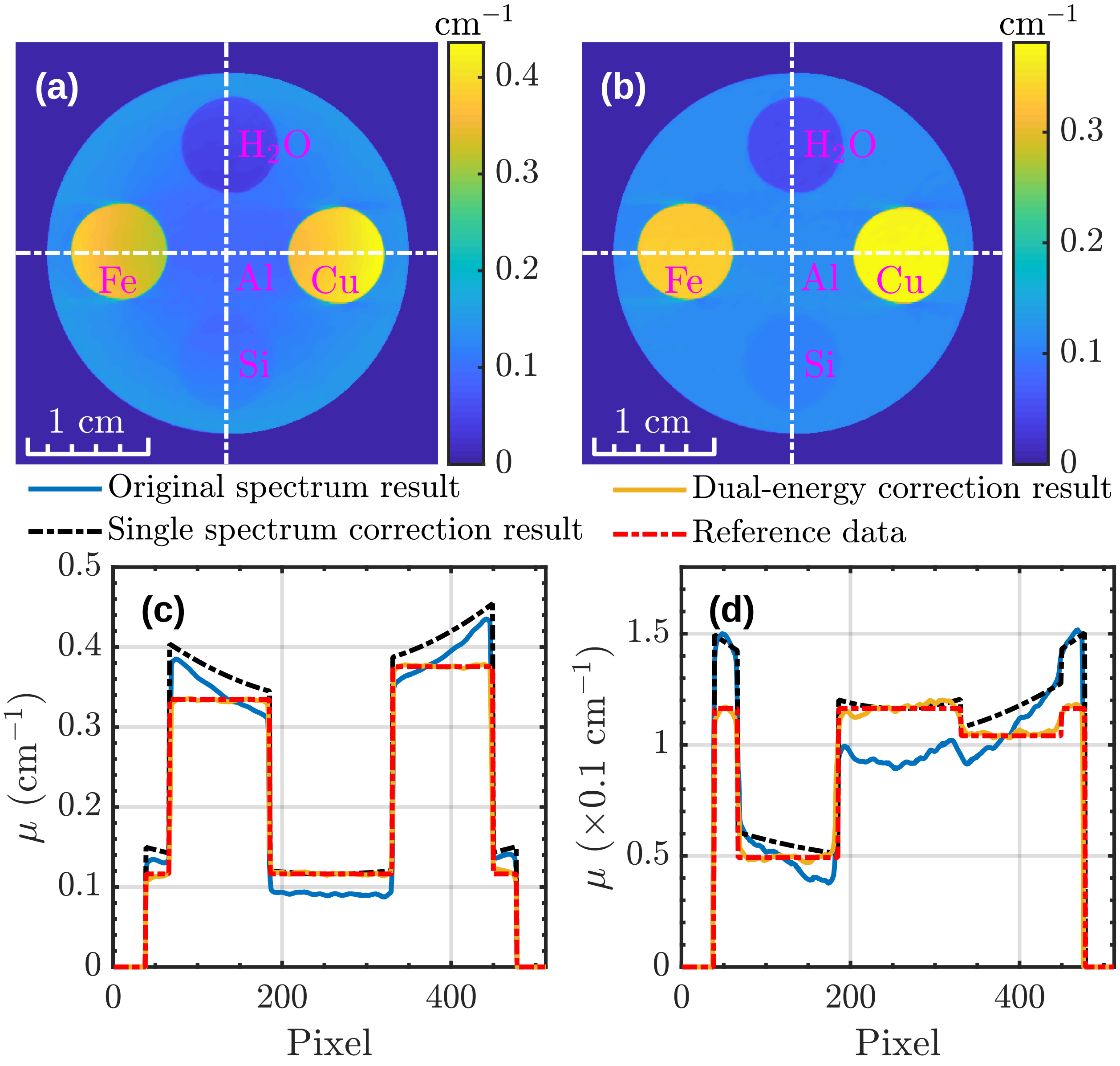

Fig. 4. CT reconstruction results of the imaging object: (a) direct reconstruction using the original energy-angle correlation spectrum at gamma-ray peak energy of 2 MeV; (b) monochromatic reconstruction at gamma-ray energy of 2 MeV using the dual-energy scan scheme; (c) and (d) illustrate, respectively, the horizontal and vertical center profiles [white dotted lines in (a) and (b)] of the reconstruction images.

To obtain ρ_e and Z_{eff}, the values of c_1 and c_2 are required, and they can be calculated either by directly reconstructing Eq. (8) or solving Eq. (4) at two different gamma-ray energies. Distinguished by whether $\mu(E)$ reconstruction is required, the reconstruction of c_1 and c_2 can be realized by either pre-processing or post-processing methods. In the pre-processing method, c_1 and c_2 are reconstructed based on the projection data C_1 and C_2 calculated by solving Eq. (7). In the post-processing method, monochromatic CT of the imaging object should be firstly reconstructed at two different gamma-ray energies E_{H} (e.g., 4 MeV) and E_{L} (e.g., 2 MeV), and then c_1 and c_2 are calculated by solving Eq. (4) at the two gamma-ray energies E_{H} and E_{L}.

III. RESULTS AND DISCUSSIONS

The basis materials chosen for the CT reconstruction of the imaging object were iron (Fe) and carbon (C), whose linear attenuation coefficients can be found in the National Institute of Standards and Technology (NIST) [57]. The CT reconstruction results of the imaging object using the original energy-angle correlation spectrum with gamma-ray peak energy of 2 MeV and the monochromatic CT reconstruc-

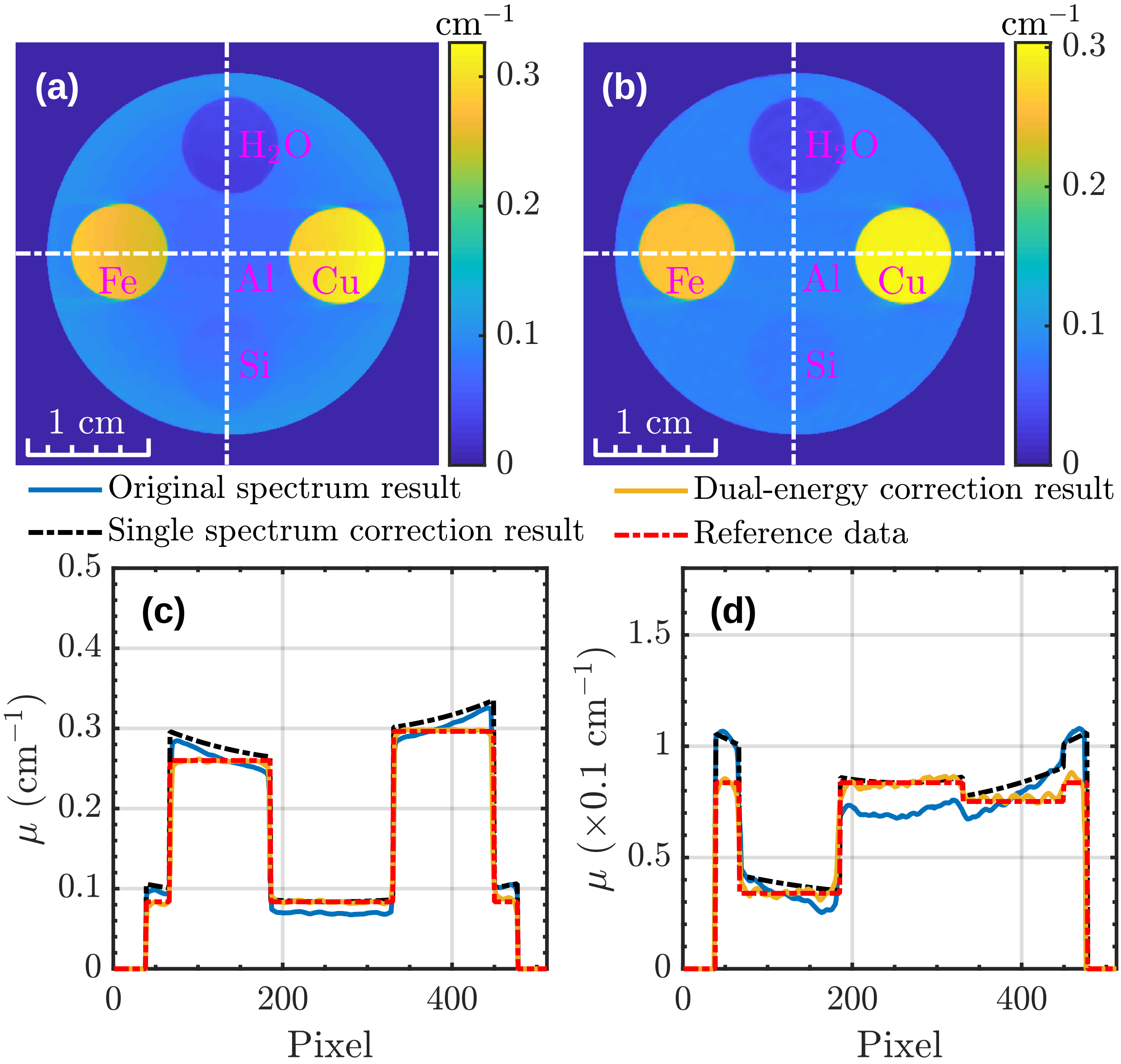

Fig. 5. CT reconstruction results of the imaging object: (a) direct reconstruction using the original energy-angle correlation spectrum at gamma-ray peak energy of 4 MeV; (b) monochromatic reconstruction at gamma-ray energy of 4 MeV using the dual-energy scan scheme; (c) and (d) illustrate, respectively, the horizontal and vertical center profiles [white dotted lines in (a) and (b)] of the reconstruction images.

tion results at gamma-ray energy of 2 MeV using the dual-energy scan scheme are illustrated in Figs. 4(a) and 4(b), respectively. To avoid the Mosaic phenomenon in the CT reconstruction image caused by under-sampling and obtain a smooth reconstruction result, 512 $\times$ 512 pixels were chosen in the CT reconstruction region, which leads to a virtual resolution much higher than the practical one of the transmission detector. For quantitative comparison, the horizontal and vertical center profiles of the reconstruction results are shown in Figs. 4(c) and 4(d), respectively. Meanwhile, the similar CT reconstruction results at gamma-ray energy of 4 MeV are illustrated in Fig. 5. Owing to the influence of the energy-angle correlation spectra, there are obvious "cupping artifacts" appearing in the reconstruction images. Using the dual-energy scan scheme described in Section II A, those "cupping artifacts" can be perfectly corrected, and the reconstructed linear attenuation coefficient of the imaging object agrees well with its theoretical value, as shown in Figs. 4(c), 4(d), 5(c), and 5(d). Considering that the gamma-ray energy is correlated with the detection angle, different parts of the imaging object will be irradiated by gamma-rays with different energy. The energy-modified linear attenuation coefficient of the imaging object, which gives the theoretical $\mu(E)$ of the imaging object with the gamma-ray energy E calculated based on the energy-angle correlation relation Eq. (1), is also illustrated in Figs. 4(c), 4(d), 5(c), and 5(d) using black dotted lines. The

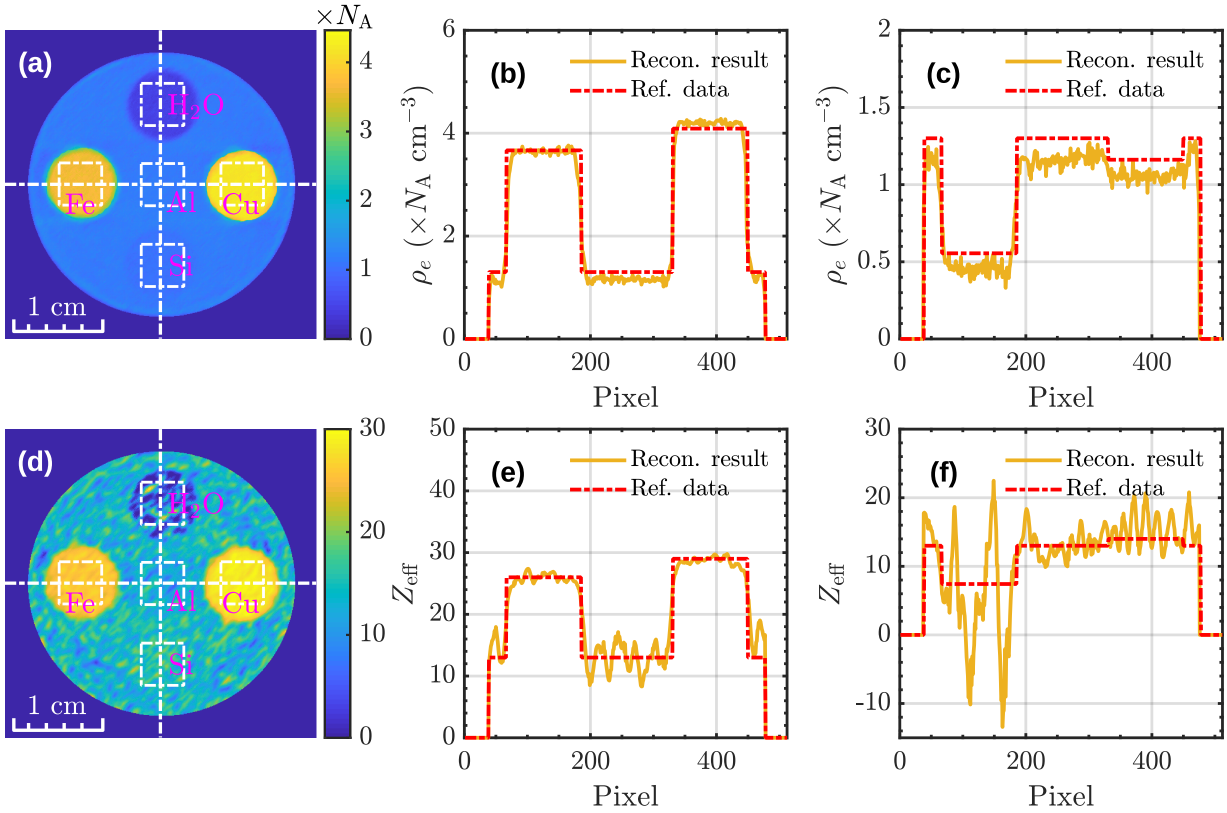

Fig. 6. Electron density and effective atomic number of the imaging object reconstructed using the pre-processing method: (a) ρ_e image; (b) and (c) illustrate, respectively, the horizontal and vertical center profiles of (a); (d) Z_{eff} image; (e) and (f) illustrate, respectively, the horizontal and vertical center profiles of (d). The white dotted squares in (a) and (d) are ROIs chosen for quantitative analysis of the reconstruction results.

energy-modified linear attenuation coefficient of the imaging object exhibits a similar variation tendency as the reconstruction result using the original energy-angle correlation spectrum that the linear attenuation coefficient for the same material increases with the radius. However, a quantitative comparison shows that the two results does not agree well, particularly around the center of the imaging object. Therefore, the single spectrum correction using the energy-angle correlation information Eq. (1) cannot reflect the practical reconstruction result.

The electron density and effective atomic number of the imaging object reconstructed using the pre-processing and post-processing methods are shown in Figs. 6 and 7, respectively. For both reconstruction methods, the reconstruction quality of electron density is much better than the counterpart of effective atomic number, which can be attributed to the division operation in Eq. (12b). Compared with the pre-processing method, there are serious artifacts around the boundaries of H_2O, Fe, and Cu in Z_{eff} image reconstructed using the post-processing method.

To quantitatively evaluate the reconstruction quality of the two methods, five regions-of-interest (ROIs) illustrated in Figs. 6(a), 6(d), 7(a), and 7(d) using white dotted squares are chosen. The ρ_e and Z_{eff} reconstruction results of the five materials are shown in Tables 1 and 2, respectively. For the reconstruction value in Tables 1 and 2, both the mean value and its standard error calculated over the ROI are given. In terms of ρ_e, the precision (standard error) of the five materials reconstructed using the post-processing method is much higher than that reconstructed using the pre-processing method. Meanwhile, the accuracy (relative error) of ρ_e reconstructed using the post-processing method is slightly higher than that reconstructed using the pre-processing method for all materials except for Cu. In terms of Z_{eff}, the reconstruction precision using the post-processing method is slightly lower than that using the pre-processing method for all materials except for H_2O, and the reconstruction accuracy using the post-processing method is almost similar with that using the pre-processing method for all materials except for H_2O. Therefore, it is more suitable for ρ_e reconstruction using the post-processing method and Z_{eff} reconstruction using the pre-processing method. For moderate-Z materials (e.g., Fe and Cu), excellent reconstruction is obtained with accuracy less than 3% and 1.5% for ρ_e and Z_{eff}, respectively. For Fe, the relative error of ρ_e and Z_{eff} is the smallest, and this was to be expected since Fe is one of the basis material. For relatively low-Z materials (e.g., Al, Si, H_2O), the lower ρ_e reconstruction accuracy may be attributed to the less accurate basis material decomposition of linear attenuation coefficient. Basis material decomposition models with higher accuracy need to

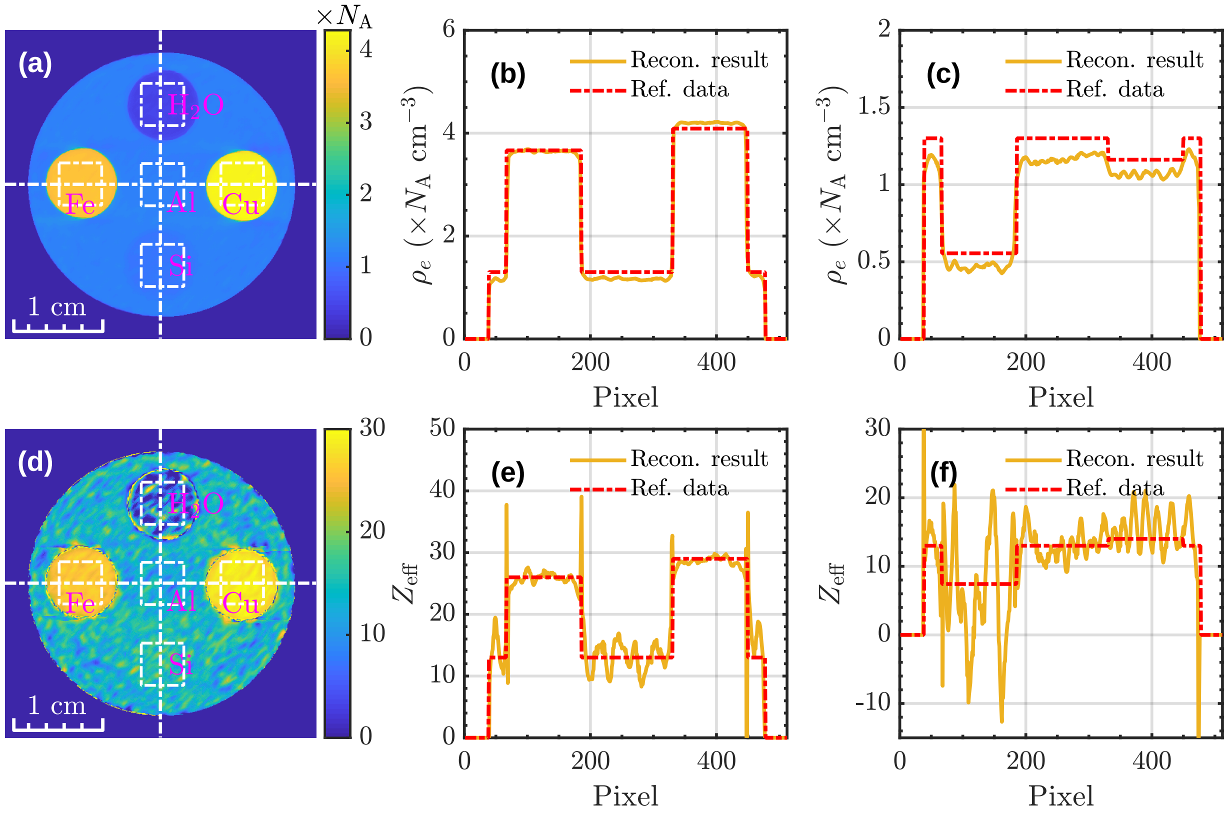

Fig. 7. Electron density and effective atomic number of the imaging object reconstructed using the post-processing method: (a) ρ_e image; (b) and (c) illustrate, respectively, the horizontal and vertical center profiles of (a); (d) Z_{eff} image; (e) and (f) illustrate, respectively, the horizontal and vertical center profiles of (d). The white dotted squares in (a) and (d) are ROIs chosen for quantitative analysis of the reconstruction results.

TABLE 1. Reconstructed electron density ρ_e of the imaging object.

Material	Reference value ($\times N_A$ cm^{-3})	Pre-processing		Post-processing	
		Reconstruction value ($\times N_A$ cm^{-3})	Relative error (%)	Reconstruction value ($\times N_A$ cm^{-3})	Relative error (%)
Al	1.300	1.159±0.097	10.89	1.164±0.023	10.47
Si	1.162	1.053±0.092	9.35	1.063±0.016	8.50
H_2O	0.555	0.461±0.099	16.92	0.470±0.020	15.35
Fe	3.666	3.651±0.088	0.42	3.654±0.023	0.32
Cu	4.089	4.196±0.093	2.62	4.198±0.023	2.67

TABLE 2. Reconstructed effective atomic number Z_{eff} of the imaging object.

Material	Reference value	Pre-processing		Post-processing	
		Reconstruction value	Relative error (%)	Reconstruction value	Relative error (%)
Al	13	12.58±2.69	3.21	12.66±2.88	2.58
Si	14	15.39±2.50	9.91	15.42±2.78	10.16
H_2O	7.42	6.54±9.01	11.83	7.14±8.65	3.74
Fe	26	25.94±0.79	0.26	25.93±0.82	0.28
Cu	29	28.68±0.76	1.09	28.69±0.78	1.07

be developed in future studies to improve the reconstruction accuracy of ρ_e. Besides, the gamma-ray energy chosen for the dual-energy scan may be another reason that causes the high relative error of ρ_e and Z_{eff} reconstruction for those low-Z materials. Since gamma-ray energies of 2 and 4 MeV are too high for low-Z materials in the imaging object, the statistic error of monochromatic CT reconstruction is relatively high, as shown in Figs. 4(d) and 5(d), which finally causes the high

relative error of ρ_e and Z_{eff} reconstruction. To reduce the relative error of ρ_e and Z_{eff} caused by the choice of gamma-ray energy for dual-energy scan, the photon number used for the MC simulation should be increased or the gamma-ray energy should be reduced. Although the pre-processing method for Z_{eff} reconstruction has advantage over the post-processing method in terms of boundary artifacts suppression and high-precision reconstruction, the reconstruction precision of Z_{eff}, owing the division operation in Eq. (12b), is much lower than that of ρ_e. Therefore, effective reconstruction methods need to be developed to improve the reconstruction precision of Z_{eff}.

Since the FOV using the dual-energy scan scheme, compared with the quasi-monochromatic scan ("translation + rotation" scheme), is increased more than 7-fold, the imaging time using the dual-energy scan scheme (only "rotation" is needed), when the CT scans using different gamma-ray energy are carried out separately, can be reduced by at least 3.5 times. However, dual-color gamma-rays can be easily produced simultaneously for an ICS light source [58–60] by using one of the following three schemes: (i) dual-color lasers interacting with the same electron beam; (ii) single-color laser interacting with the same electron beam at different interaction angles by beam splitting; (iii) dual-color electron beams interacting with the same laser. Using the dual-color gamma-rays, the dual-energy scan can be realized simultaneously by combining with a layered transmission detector (the front layer for low-energy gamma-ray detection and the rear layer for high-energy gamma-ray detection, as in the case of early dual-energy CT [61, 62]). Therefore, the imaging time can be further reduced by 2 times. Another advantage of the dual-energy scan scheme, compared with the quasi-monochromatic scan, is that the ρ_e and Z_{eff} of the imaging object can be obtained at the same time.

IV. CONCLUSION

Quasi-monochromatic, continuously energy-tunable, and high-brightness gamma-rays produced by inverse Compton scattering (ICS) light sources can fundamentally resolve the beam hardening artifacts in computed tomography (CT) reconstruction, which can help promote the accuracy of quantitative analysis and inspection in CT-based dimensional metrology. To improve the imaging efficiency of gamma-ray CT based on this type of light source, an effective method for large field-of-view (FOV) imaging was developed. Using dual-energy scan scheme, the influence of intrinsic energy-angle correlation spectrum of ICS light sources on CT reconstruction was resolved, and monochromatic CT of the imaging object was accurately reconstructed. Furthermore, the electron density ρ_e and effective atomic number Z_{eff} of the imaging object can also be obtained. For ρ_e reconstruction, the post-processing method has obvious advantage over the pre-processing method; for Z_{eff} reconstruction, however, the pre-processing method is preferred.

[1] K.V. Wong and A. Hernandez, A review of additive manufacturing. Int. Sch. Res. Notices **2012**, 1-10 (2012). doi: 10.5402/2012/208760

[2] W. Gao, Y.B. Zhang, D. Ramanujan et al, The status, challenges, and future of additive manufacturing in engineering. Comput. Aided Des. **69**, 65-89 (2015). doi: 10.1016/j.cad.2015.04.001

[3] J.P. Kruth, M. Bartscher, S. Carmignato et al, Computed tomography for dimensional metrology. CIRP Ann. - Manuf. Technol. **60**, 821-842 (2011). doi: 10.1016/j.cirp.2011.05.006

[4] L. De Chiffre, S. Carmignato, J.-P. Kruth et al, Industrial applications of computed tomography. CIRP Ann. - Manuf. Technol. **63**, 655-677 (2014). doi: 10.1016/j.cirp.2014.05.011

[5] M. Ferrucci, R.K. Leach, C. Giusca et al, Towards geometrical calibration of x-ray computed tomography-a review. Meas. Sci. Technol. **26**, 092003 (2015). doi: 10.1088/0957-0233/26/9/092003

[6] H. Villarraga-Gómez, E.L. Herazo, S.T. Smith, X-ray computed tomography: from medical imaging to dimensional metrology. Precis. Eng. **60**, 544-569 (2019). doi: 10.1016/j.precisioneng.2019.06.007

[7] M. Bartscher, U. Hilpert, J. Goebbels et al, Enhancement and proof of accuracy of industrial computed tomography (CT) measurements. CIRP Ann. **56**, 495-498 (2007). doi: 10.1016/j.cirp.2007.05.118

[8] W. Dewulf, Y. Tan, K. Kiekens, Sense and non-sense of beam hardening correction in CT metrology. CIRP Ann. - Manuf. Technol. **61**, 495-498 (2012). doi: 10.1016/j.cirp.2012.03.013

[9] X. Zhang, L. Li, F. Zhang, et al, Improving the accuracy of CT dimensional metrology by a novel beam hardening correction method. Meas. Sci. Technol. **26**, 015007 (2014). doi: 10.1088/0957-0233/26/1/015007

[10] Y. Tan, K. Kiekens, F. Welkenhuyzen et al, Simulation-aided investigation of beam hardening induced errors in CT dimensional metrology. Meas. Sci. Technol. **25**, 064014 (2014). doi: 10.1088/0957-0233/25/6/064014

[11] J.J. Lifton, A.A. Malcolm, J.W. McBride, An experimental study on the influence of scatter and beam hardening in x-ray CT for dimensional metrology. Meas. Sci. Technol. **27**, 015007 (2015). doi: 10.1088/0957-0233/27/1/015007

[12] G.T. Herman, Correction for beam hardening in computed tomography. Phys. Med. Biol. **24**, 81 (1979). doi: 10.1088/0031-9155/24/1/008

[13] H.W. Gao, L. Zhang, Z.Q. Chen et al, Beam hardening correction for middle-energy industrial computerized tomography. IEEE Trans. Nucl. Sci. **53**, 2796-2807 (2006). doi: 10.1109/TNS.2006.879825

[14] X.Q. Mou, S.J. Tang, H.Y. Yu, A beam hardening correction method based on HL consistency. Proc. SPIE **6318**, 583-592 (2006). doi: 10.1117/12.682869

[15] Y.B. Zhang, X.Q. Mou, S.J. Tang, Beam hardening correction for fan-beam CT imaging with multiple materials. IEEE NSS MIC, 3566-3570 (2010). doi: 10.1109/NSS-MIC.2010.5874473

[16] S.J. Tang, X.Q. Mou, Q. Xu et al, Data consistency condition–based beam-hardening correction. Opt. Eng. **50**, 076501 (2011). doi: 10.1117/1.3599869

[17] S.J. Tang, K.D. Huang, Y.Y. Cheng et al, Optimization based beam-hardening correction in CT under data integral invariant constraint. Phys. Med. Biol. **63**, 135015 (2018). doi: 10.1088/1361-6560/aaca14

[18] W. Zhao, G.T. Fu, C.L. Sun et al, Beam hardening correction for a cone-beam CT system and its effect on spatial resolution. Chinese Phys. C **35**, 978 (2011). doi: 10.1088/1674-1137/35/10/018

[19] S.H. Luo, H.Z. Wu, Y. Sun et al, A fast beam hardening correction method incorporated in a filtered back-projection based MAP algorithm. Phys. Med. Biol. **62**, 1810 (2017). doi: 10.1088/1361-6560/aa56b5

[20] M. Kachelrieß, K. Sourbelle, W.A. Kalender, Empirical cupping correction: A first-order raw data precorrection for cone-beam computed tomography. Med. Phys. **33**, 1269-1274 (2006). doi: 10.1118/1.2188076

[21] M. Abella, C. Martínez, M. Desco et al, Simplified statistical image reconstruction for X-ray CT with beam-hardening artifact compensation. IEEE Trans. Med. Imaging **39**, 111-118 (2019). doi: 10.1109/TMI.2019.2921929

[22] J.A. O'Sullivan, J. Benac, Alternating minimization algorithms for transmission tomography. IEEE Trans. Med. Imaging **26**, 283-297 (2007). doi: 10.1109/TMI.2006.886806

[23] R. Alvarez and A. Macowski, Energy-selective reconstructions in x-ray computerized tomography. Phys. Med. Biol. **21**, 733–744 (1976). doi: 10.1088/0031-9155/21/5/002

[24] J.P. Stonestrom, R.E. Alvarez, A. Macovski, A framework for spectral artifact corrections in X-ray CT. IEEE Trans. Biomed. Eng. **2**, 128-141 (1981). doi: 10.1109/TBME.1981.324786

[25] Y. Censor, T. Elfving, G.T. Herman et al, A method of iterative data refinement and its applications. Math. Methods Appl. Sci. **7**, 108-123 (1985). doi: 10.1002/mma.1670070108

[26] J. Hsieh, R.C. Molthen, C.A. Dawson et al, An iterative approach to the beam hardening correction in cone beam CT. Med. Phys. **27**, 23-29 (2000). doi: 10.1118/1.598853

[27] G. Van Gompel, K. Van Slambrouck, M. Defrise et al, Iterative correction of beam hardening artifacts in CT. Med. Phys. **38**, S36-S49 (2011). doi: 10.1118/1.3577758

[28] L. Brabant, E. Pauwels, M. Dierick et al, A novel beam hardening correction method requiring no prior knowledge, incorporated in an iterative reconstruction algorithm. NDT & E Int. **51**, 68-73 (2012). doi: 10.1016/j.ndteint.2012.07.002

[29] C.X. Tang, W.H. Huang, R.K. Li et al, Tsinghua Thomson scattering X-ray source. Nucl. Instrum. Methods Phys. Res., Sect. A **608**, S70–S74 (2009). doi: 10.1016/j.nima.2009.05.088

[30] X.C. Lin, H. Zha, J.R. Shi et al, Development of a seven-cell S-band standing-wave RF-deflecting cavity for Tsinghua Thomson scattering X-ray source. Nucl. Sci. Tech. **32**, 36 (2021). doi: 10.1007/s41365-021-00871-5

[31] H.W. Wang, G.T. Fan, L.X. Liu et al, Commissioning of laser electron gamma beamline SLEGS at SSRF. Nucl. Sci. Tech. **33**, 87 (2022). doi: 10.1007/s41365-022-01076-0

[32] X. Pang, B.H. Sun, L.H Zhu et al, Progress of photonuclear cross sections for medical radioisotope production at the SLEGS energy domain. Nucl. Sci. Tech. **34**, 187 (2023). doi: 10.1007/s41365-023-01339-4

[33] L.X. Liu, H.W. Wang, G.T. Fan et al, The SLEGS beamline of SSRF. Nucl. Sci. Tech. **35**, 111 (2024). doi: 10.1007/s41365-024-01469-3

[34] K. Achterhold, M. Bech, S. Schleede et al, Monochromatic computed tomography with a compact laser-driven X-ray source. Sci. Rep. **3**, 1313 (2013). doi: 10.1038/srep01313

[35] Z.J. Chi, Y.C. Du, W.H. Huang et al, Energy-angle correlation correction algorithm for monochromatic computed tomography based on Thomson scattering X-ray source. J. Appl. Phys. **122**, 234903 (2017). doi: 10.1063/1.4996324

[36] Z.J. Chi, Y.C. Du, L.X. Yan et al, Experimental feasibility of dual-energy computed tomography based on the Thomson scattering X-ray source. J. Synchrotron Radiat. **25**, 1797-1802 (2018). doi: 10.1107/S1600577518012663

[37] S. Kulpe, M. Dierolf, B. Günther et al, Spectroscopic imaging at compact inverse Compton X-ray sources. Phys. Med. **79**, 137-144 (2020). doi: 10.1016/j.ejmp.2020.11.015

[38] M. Bech, O. Bunk, C. David et al, Hard X-ray phase-contrast imaging with the Compact Light Source based on inverse Compton X-rays. J. Synchrotron Radiat. **16**, 43-47 (2009). doi: 10.1107/S090904950803464X

[39] E. Eggl, S. Schleede, M. Bech et al, X-ray phase-contrast tomography with a compact laser-driven synchrotron source. Proc. Natl. Acad. Sci. **112**, 5567-5572 (2015). doi: 10.1073/pnas.1500938112

[40] Z. Zhang, Y.C. Du, L.X. Yan et al, In-line phase-contrast imaging based on Tsinghua Thomson scattering x-ray source. Rev. Sci. Instrum. **85**, 083307 (2014). doi: 10.1063/1.4893658

[41] Z.J. Chi, L.X. Yan, Y.C. Du et al, Recent progress of phase-contrast imaging at Tsinghua Thomson-scattering X-ray source. Nucl. Instrum. Methods Phys. Res., Sect. B **402**, 364-369 (2017). doi: 10.1016/j.nimb.2017.02.062

[42] J.Y. Sun, Z.J. Chi, Y.C. Du et al, A simulation method of gamma-ray phase contrast imaging for metal samples. Nucl. Instrum. Methods Phys. Res., Sect. A **1053**, 168321 (2023). doi: 10.1016/j.nima.2023.168321

[43] Z.J. Chi, Y.C. Du, W.H. Huang et al, Linearly polarized X-ray fluorescence computed tomography based on a Thomson scattering light source: a Monte Carlo study. J. Synchrotron Radiat. **27**, 737-745 (2020). doi: 10.1107/S1600577520003574

[44] Y. Taira, S. Endo, S. Kawamura et al, Measurement of the spatial polarization distribution of circularly polarized gamma rays produced by inverse Compton scattering. Phys. Rev. A **107**, 063503 (2023). doi: 10.1103/PhysRevA.107.063503

[45] H.S. Zen, H. Ohgaki, Y. Taira et al, Demonstration of tomographic imaging of isotope distribution by nuclear resonance fluorescence. AIP Adv. **9**, 035101 (2019). doi: 10.1063/1.5064866

[46] K. Ali, H. Ohgaki, H.S. Zen et al, Selective isotope CT imaging based on nuclear resonance fluorescence transmission method. IEEE Trans. Nucl. Sci. **67**, 1976-1984 (2020). doi: 10.1109/TNS.2020.3004565

[47] H.Y. Lan, T. Song, Z.H. Luo et al, Isotope-sensitive imaging of special nuclear materials using computer tomography based on scattering nuclear resonance fluorescence. Phys. Rev. Appl. **16**, 054048 (2021). doi: 10.1103/PhysRevApplied.16.054048

[48] H.Y. Lan, T. Song, J.L. Zhang et al, Rapid interrogation of special nuclear materials by combining scattering and transmission nuclear resonance fluorescence spectroscopy. Nucl. Sci. Tech. **32**, 84 (2021). doi: 10.1007/s41365-021-00914-x

[49] M. Omer, T. Shizuma, R. Hajima et al, Nondestructive determination of isotopic abundance using multi-energy nuclear resonance fluorescence driven by laser Compton scattering source. J. Appl. Phys. **135**, 184903 (2024). doi: 10.1063/5.0197076

[50] S.K. Ride, E. Esarey, M. Baine, Thomson scattering of intense lasers from electron beams at arbitrary interaction angles. Phys. Rev. E **52**, 5425 (1995). doi: 10.1103/PhysRevE.52.5425

[51] Y.X. Xing, L. Zhang, X.H. Duan et al, A reconstruction method for dual high-energy CT with MeV X-rays. IEEE Trans. Nucl.

Sci. **58**, 537-546 (2011). doi: 10.1109/TNS.2011.2112779

[52] S. Agostinelli, J. Allison, K.A. Amako et al., GEANT4—a simulation toolkit. Nucl. Instrum. Methods Phys. Res., Sect. A **506**, 250 (2003). doi: 10.1016/S0168-9002(03)01368-8

[53] Y.C. Du, H. Chen, H.Z. Zhang et al., A very compact inverse Compton scattering gamma-ray source. High Power Laser and Particle Beams **34**, 104010 (2022). doi: 10.11884/HPLPB202234.220132

[54] X.C. Lin, H. Zha, J.R. Shi et al., Design, fabrication, and testing of low-group-velocity S-band traveling-wave accelerating structure. Nucl. Sci. Tech. **33**, 147 (2022). doi: 10.1007/s41365-022-01124-9

[55] Q. Gao, H. Zha, J.R. Shi et al., Design and test of an X-band constant gradient structure. Phys. Rev. Accel. Beams **27**, 090401 (2024). doi: 10.1103/PhysRevAccelBeams.27.090401

[56] See https://www-jlc.kek.jp/ tauchi/index/cain/non-linearQED/CainMan242.pdf for "User's Manual of CAIN, Version 2.42" (last accessed March 29, 2024).

[57] See https://www.nist.gov/pml/x-ray-mass-attenuation-coefficients for the linear attenuation coefficient data of different materials (last accessed April 9, 2024).

[58] V. Petrillo, A. Bacci, C. Curatolo et al., Dual color x rays from Thomson or Compton sources. Phys. Rev. ST Accel. Beams **17**, 020706 (2014). doi: 10.1103/PhysRevSTAB.17.020706

[59] I. Drebot, V. Petrillo, and L. Serafini, Two-colour X-gamma ray inverse Compton back-scattering source. EPL **120**, 14002 (2017). doi: 10.1209/0295-5075/120/14002

[60] Y. Wu, C.H. Yu, Z.Y. Qin et al, Dual-color γ-rays via all-optical Compton scattering from a cascaded laser-driven wakefield accelerator. Plasma Phys. Control. Fusion **61**, 085030 (2019). doi: 10.1088/1361-6587/ab29d9

[61] T. Ishigaki, S. Sakuma, and M. Ikeda, One-shot dual-energy subtraction chest imaging with computed radiography: clinical evaluation of film images. Radiology **168**, 67–72 (1988). doi: 10.1148/radiology.168.1.3289096

[62] B.K. Stewart and H.K. Huang, Single-exposure dual-energy computed radiography. Med. Phys. **17**, 866–875 (1990). doi: 10.1118/1.596479